PCCP

Dynamics and Molecular Interactions of Single-stranded DNA in Nucleic Acid Biosensors with Varied Surface Properties

Journal:	*Physical Chemistry Chemical Physics*
Manuscript ID	CP-ART-04-2019-002441.R1
Article Type:	Paper
Date Submitted by the Author:	01-Jun-2019
Complete List of Authors:	Cholko, Timothy; University of California Riverside, Chemistry Kaushik, Shivansh; University of California Riverside, Chemistry Chang, Chia-en; University of California, Riverside, Chemistry

Dynamics and Molecular Interactions of Single-stranded DNA in Nucleic Acid Biosensors with Varied Surface Properties

Timothy Cholko, Shivansh Kaushik, and Chia-en A. Chang*

Department of Chemistry, University of California, Riverside, Riverside, CA 92521
Telephone: (951) 827-7263
Email: chiaenc@ucr.edu

Abstract

Electrochemical DNA biosensors utilizing self-assembled monolayers (SAMs) with inserted DNA probes are a promising biosensor design because of their ease of preparation, miniaturization, and tunability. However, much is still unknown about the interactions between biomolecules such as DNA and various surfaces. A fundamental question regarding these sensors concerns the nature of diffusion of target molecules taking place on sensor surfaces and whether it speeds up the molecular recognition process. Lack of understanding of molecular interaction and surface diffusion in addition to questions regarding the behavior of DNA probes immobilized on these surfaces currently limits the rational design of nucleic acid biosensors. Using all-atom unbiased molecular dynamics (MD) simulations we found that single-stranded DNA (ssDNA) behavior on SAMs is drastically altered by different surface chemistries, with ssDNA adopting very different orientations upon adsorption and surface diffusivity varying over an order of magnitude. Probe behavior varies equally broadly as probes are considerably more stable in certain SAMs than others, which affects the accessibility of probes to the target molecules and likely changes DNA hybridization kinetics in multiple ways. We also found that nearby probes can alter each other's orientations substantially, which highlights the importance of surface density control. Our results elucidate nucleic acid biosensor dynamics vital to rational design and offer insights that can aid in the design of surface properties and patterning for specific applications.

Introduction

Electrochemical DNA biosensors employing a self-assembled monolayers (SAM) of functionalized alkanethiols on gold or other substrates have proven to be excellent designs for detecting a wide range of biomarkers because of their ease of preparation, tunability, and miniaturization, and their greater efficiency and accuracy than current techniques.[1–4] In this work, we studied an electrochemical DNA biosensor in which immobilized single-stranded DNA (ssDNA) inserted into the SAM acts as a probe for its complementary sequence.[5–8] The SAM consists of an alkane chain with a thiol head group at one end by which it bonds to the gold and a functional tail group at the other end that is exposed to the solvent. The choice of tail group largely controls the surface properties of the SAM and can be selected to suit a number of possible applications, for example, adsorption or repulsion of specific molecules such as proteins or ions, channeling of substrates or target molecules, modeling charged biological surfaces[9–13], and immobilization of DNA for controlled assembly.[14–16] The sensor works by detecting hybridization – the formation of double-

stranded DNA out of two complimentary single strands – of target DNA sequences with the attached probes, which may occur as targets diffuse through the solvent or across the SAM surface.

Currently, experimental techniques yield limited information about the important dynamics and mechanisms of these sensors. Surface plasmon resonance, atomic force microscopy, and electrochemical measurements[17–20] have been used to study the behavior of DNA on SAMs, but all have the drawback of detecting only the hybridized double-stranded DNA and provide little to no information about the mechanism of hybridization. Additionally, current techniques for classifying the structure of SAMs, which plays a major role in determining the nature of DNA–SAM interactions, lack the resolution to describe nanoscale and sub-nanoscale features.[21–22] Computational studies can help fill in these gaps in knowledge, but thus far have mainly been used to elucidate the interactions of SAMs with water[23–27] or proteins.[28–32] Computational studies of DNA interactions with SAMs have been less common. Park and Aluru studied ssDNA on PEG-silane surfaces, measuring diffusion coefficients and conformations of adsorbed DNA[33], and Elder and Jayaraman used umbrella sampling to study ssDNA diffusion and interaction with OEG and OMe SAMs.[34]

An important outstanding question regarding sensors of this sort pertains to the amount of 2-dimensional (2-D) hybridization, that is, diffusion of target DNA along the SAM leading to hybridization, versus the amount of 3-dimensional (3-D) hybridization, in which hybridization occurs *via* diffusion of targets through the solvent directly to probes. If 2-D hybridization makes a significant contribution, the interaction of DNA with the surface and therefore the surface properties of the SAM become extremely important. The question of 2-D versus 3-D diffusion is relevant in many fields in addition to biosensing. Chemical separations using membranes may make use of subtle differences in 2-D diffusion of different molecules[35]. Genotyping and gene expression profiling take advantage of DNA microarrays utilizing special surfaces[36–37], and catalysis may utilize surfaces with immobilized catalysts to enhance reaction rates[38]. Therefore, knowledge of DNA's behavior on surfaces, whether diffusing or immobilized, is likely very applicable to an extremely wide array of disciplines.[39]

Moreover, many unanswered questions remain about the dynamics and organization of the DNA probes on SAMs. For example, heterogeneity in surface concentration of inserted DNA probes has been observed, and these differences in concentration may have a substantial effect on molecular recognition between the target and probe.[21] Moreover, the nature of hybridization is believed to be much more complicated at a surface than in bulk solution because of the unique thermodynamic environment of probes concentrated on a surface.[40–41] Interaction between probes and the monolayer and between nearby individual probes can affect their ability to hybridize with incoming target strands. Understanding the effect of all these factors on behavior of DNA on various surfaces can help steer rational design of nucleic acid biosensors.

In this study we performed four sets of MD simulations for several different systems which model various important aspects of the biosensor's structure and function with multiple surface chemistries. One set of simulations aimed at understanding the dynamics and intermolecular

interactions of an ssDNA probe inserted into the SAMs (Fig. 1a). Another set of simulations studied the diffusion of an ssDNA target molecule and its interaction with the SAMs from two different starting distances (Fig. 1b and c). Finally, we investigated the effect of having multiple probes in close proximity by simulating probes inserted into SAMs at three different inter-probe distances (Fig. 1d).

Simulation Methods & Analysis

Model Systems

The biosensor was modeled with either an undecanethiol, 11-mercapto-1-undecanol, 11-amino-1-undecanethiol, or 11-mercaptoundecanoic acid SAM in order to sample a wide range of surface properties. We refer to these different SAMs as the CH_3–, OH–, NH–, or COO–SAM, respectively. Hexadecane versions of those four SAMs were also simulated in some cases, so we refer to the two different lengths as C11 or C16 (Fig. 2). The chains have a hexagonal packing pattern and a packing density on the order of $10^{14}/cm^2$ which gives an average nearest-neighbor distance of 4.98 Å. All chains were started with a lean 30° from the surface normal, a twist of 55° around their long axis, and rotation 15° around the surface normal corresponding to the lowest-energy conformation of alkanethiol SAMs on Au(111) described by Schreiber.[42] The gold substrate was modeled as a one-atom-thick Au(111) surface onto which the alkanethiol chains were attached via an Au-S bond. All atoms were mobile during simulation except the gold.

MD Simulation Parameters

All-atom unbiased MD simulations were performed by the NAMD 2.12 package[43] with the AMBER FF14SB force field[44] used to model the DNA and the AMBER GAFF force field[45] for the SAM and gold. A 12 Å cutoff for electrostatics was used with PME to calculate long-range electrostatics under 3-D periodic boundary conditions. Simulations used explicit TIP3P water molecules and explicit Na^+ or Cl^- ions to achieve a neutral charge in the simulation box. For the target simulations, this resulted in an ionic concentration of approximately 0.010 M with the OH– and CH3–SAMs (7 Na^+ ions), 0.340 M with the NH–SAM (241 Cl^- ions), and 1.09 M with the COO–SAM (756 Na^+ ions). For probe simulations, ionic concentrations were approximately 0.019 M with the OH– and CH3–SAMs (28 Na^+ ions), 0.167 with the NH–SAM (248 Cl^- ions), and 0.516 M with the COO–SAM (771 Na^+ ions). Gold atoms in all models were uncharged. The functionalized alkanethiols in the various SAMs were parameterized in AMBER's *antechamber* program with partial atomic charges assigned by the AM1-BCC method.[46] Systems were minimized in three steps: first just the water and ions, then the water and SAM, followed by the entire system at once. This was followed by two stages of equilibration using a 1 fs timestep: first water and ions only, then the entire system. Water and ion equilibration was performed at 200, 250, 275 and 298K for 20 ps at each temperature and full system equilibration was performed at 200, 250, and 275K for 50 ps and 298K for 100 ps in the NPT ensemble. Production simulations were run in the NVT ensemble for either 50 or 100 ns. All simulations were performed twice to confirm consistency in the observed behavior, and we present data from only one simulation unless otherwise noted. Analysis of the MD trajectories was done in GROMACS 4[47] or by in-house

programs, and all visualization of trajectories and image rendering was done using VMD 1.9.2.[48–49] Further discussion of our model systems and simulation parameters is given in the ESI.

ssDNA Target Simulations

Regions of both C11 and C16 length were simulated for all four SAMs with the 8-base ssDNA sequence 5'-CGTACTGA-3' started 5Å above the SAM. In our models, 30% of the tail groups on the NH-SAM were in the protonated NH_3^+ state, and all the tail groups on the COO-SAM were in the COO^- form. A 5 Å starting distance was chosen so the ssDNA would not have to diffuse much at all before adsorbing or being repelled from a surface. We then performed simulations of the 12-base ssDNA sequence 5'-CGTACTGACTGC-3' starting 40Å above the SAM to allow it to diffuse and rotate freely to avoid biasing the simulation toward adsorption (Table 1). An approximately 125 x 135 Å slab of the SAM was modeled with the DNA centered above it and 40Å of water above the topmost atom in the DNA and at least 10Å of water below the gold substrate (ESI, Fig. S1). From these MD trajectories we obtained surface diffusion coefficients according to the Einstein relation,

$$D = \langle [r_{cm}(t) - r_{cm}(0)]^2 \rangle / 2nt$$

where r_{cm} is the position of the center of mass of the molecule, n is the dimensionality of the diffusion process, and t is the time of the diffusion process. Plots of mean square displacement (MSD) over time as well as diffusion coefficients during 10-ns subdivisions of each trajectory are given in the ESI and show that the diffusion coefficient became stable during the sampled time (Fig. S2). We also calculated the electrostatic and van der Waals (vdW) components of the ssDNA-SAM interaction energy to show the nature of ssDNA interaction with various surfaces. To calculate the vdW energy we used a 6-12 Lennard-Jones potential,

$$E_{vdW} = \left(\frac{A_{ij}}{r_{ij}^{12}} - \frac{B_{ij}}{r_{ij}^{6}}\right)$$

with $A = 4\varepsilon\sigma^{12}$ and $B = 4\varepsilon\sigma^{6}$, where ε is the potential well depth in kcal/mol, σ is the distance at which the potential is zero, and r is the distance between atoms i and j.

ssDNA Probe Simulations

ssDNA probes inserted into the four different SAMs were simulated for 100 ns using the same protonation states as described above (Table 1). The probe was 29-base ssDNA attached to a linker molecule and was the same sequence, 5'-GCTACCTCGTGAGCAGTCAGTACGTTTTT-3', in all simulations and the SAM was the same slab used in the ssDNA target simulations. These simulations were aimed at describing the behavior of probes on the different SAMs by measuring the distance maintained by the probe above the SAM surface (ESI, Fig. S3) and by tracking the probes radius of gyration (R_g) over time,

$$R_g = \sqrt{\frac{\sum_{i=1}^{N} m_i (r_i - r_{com})^2}{\sum_{i=1}^{N} m_i}}$$

where r_i is the position of atom i, r_{com} is the center-of-mass of the ssDNA, and m_i is the mass of atom i, to quantify changes from elongated to more curled conformations. All of our reported R_g values are the 3-dimensional R_g. Then, using principal component analysis[50], we decomposed probe motions into their three major components during the simulations. We also calculate electrostatic and vdW components of probe-SAM interaction energy. These simulations were 100 ns with a 1 fs timestep with at least 20Å of water above the probe tip and 15Å of water below the gold substrate.

Multiple Probe Simulations

Three simulations were performed with two probes inserted into the C11 OH-SAM. The probes were positioned 25, 50, or 100Å apart from each other to represent different possible environments on the sensor surface (Table 1). Calculations of the electrostatic interaction energy between probes were performed and we quantified changes in the dynamics of these probes compared to isolated ones by measuring the radius of gyration and distance from probe tip to SAM at each separation distance. We chose to use the OH-SAM in these simulations since it showed the least interaction with DNA and would allow probe-induced changes in dynamics to more easily discerned.

Results & Discussion

Understanding DNA's interactions with various surfaces is of vital importance in the context of biosensing. Detection of a specific sequence (the target) requires diffusion of that target sequence to one of the ssDNA probes followed by hybridization. Whether a target sequence is repelled from or adsorbed onto a surface – and the subsequent surface diffusion – profoundly affects the probability and rate of this process. Likewise, the ssDNA probes must be sterically accessible and energetically able to undergo the hybridization process, so their interactions with surfaces are of equal importance. Although all-atom MD cannot access the long time scales required to simulate the entire molecular recognition and DNA hybridization process, we have used these simulations to elucidate aspects of ssDNA dynamics on various surfaces which will strongly influence these processes. Here, we present our findings regarding the behavior of 8-base and 12-base ssDNA target sequences and the longer 29-base ssDNA probes on four different surfaces, and in some cases, two lengths, C11 and C16, of each surface (Table 1). In particular, we looked for adsorption or repulsion from a surface by tracking the ssDNA-SAM distance over time and by calculating ssDNA-SAM interaction energy. We then measured 2-D diffusion rates on each surface, analyzed the role of water and hydrogen bonding in these interactions, and used the radius of gyration of the ssDNA to quantify changes in its conformation, which may be related to surface interactions or interactions with the solvent and ions. We also measure mobility of the different SAM molecules to find any underlying patterns related to DNA diffusion or surface interactions. Finally, we used the same analyses to study the effects of high probe surface concentration which can affect hybridization by altering nearby probe orientations and conformations.

ssDNA Target Surface Interactions and Diffusion

COO–SAM From both the 5Å and 40Å starting distances, the ssDNA was initially repelled by the negatively charged COO^- tail groups of the SAM, but after a layer of Na^+ ions formed on the surface, we observed association of the ssDNA to the layer (Fig. 3a and b, 8a). This behavior is supported by our ssDNA-SAM interaction energy calculations which showed that electrostatic repulsions are dominant. However, interaction energy calculations between the ssDNA and Na^+ ions at the surface unsurprisingly show strong attraction, indicating that the ssDNA is attracted to the ionic layer and not to the SAM itself (Fig. 4a and 5a). On the C16 length, interaction between the ssDNA and SAM is near zero initially, then becomes repulsive as the ssDNA nears the SAM, attracted by the forming ionic layer. Ions have mostly adsorbed to the SAM around 20 ns, at which point the ssDNA begins to adsorb as well. The total interaction with the C16 length surface and ions dips rapidly around 35 ns of simulation when the ssDNA assumes a conformation with stronger contact with the ionic layer (red and purple, Fig. 7a). The C11 length SAM shows a similar pattern. It's clear in this case that a positively charged Na^+ layer on the surface is the reason for adsorption of ssDNA, and therefore the adsorption or repulsion of DNA to this surface will be highly dependent on the protonation state of the SAM and the ionic strength of solution. This also highlights the importance of ionic effects, especially in the case of a charged surface. We demonstrated that the ions can essentially become a property of the SAM itself and can dictate ssDNA behavior, leaving open many interesting questions for future work related to different ionic strengths in solution and protonation states of charged SAMs.

To explain the role of water in adsorption process, the amount of water–SAM hydrogen bonds (HBs) displaced upon adsorption of the ssDNA was measured and showed that ~17 fewer are present after adsorption, which may contribute unfavorably to the adsorption process (ESI, Fig. S4). It is possible that some of this is compensated by ssDNA forming its own HBs with the surface; however surprisingly, no HBs were found between the ssDNA and SAM despite the presence of many HB-capable moieties. The ssDNA is mainly associating with the ionic layer slightly above the SAM, which prevents it from approaching close enough to the SAM to form ssDNA–SAM HBs. This idea is confirmed by a close look at Figure 3a in the period of 30-50 ns, where the plot of distance to the COO–SAM is roughly 3.5-4 Å, just beyond the distance needed to form appreciable HBs. The radius of gyration (R_g) of the ssDNA shows that it's adsorbed in a highly curled backbone-out conformation, especially on the C16 SAM where we observed longer-lasting adsorption (Fig. 7a). The contact map shows that the point of closest contact is often an interior (non-end) base and shifts quite often (ESI, Fig. S5). This backbone-out conformation was also found by Monserud and Schwartz[51] and was proposed to arise from the tendency to hide the more hydrophobic bases and expose the hydrophilic backbone by forming a micelle-like structure, which is indeed what we see here (ESI, Fig. S6a). This conformational preference probably also lessens DNA's ability to form HBs with the surface.

We measured a surface diffusion coefficient (D) of 0.914 and 1.77×10^{-7} cm^2 s^{-1} on the C11 and C16 length SAMs, respectively (Table 2). This is roughly just a 3- to 6- fold decrease from that in

bulk water, likely because the ssDNA is mainly attracted to the relatively mobile Na^+ ions and not the SAM itself, yielding a slightly higher diffusion coefficient than might be expected.

OH–SAM When started 5Å above the C11 OH–SAM, the ssDNA target interacted weakly with the surface for several nanoseconds but never adsorbed and spent the majority of the simulation floating in the bulk solvent (Fig. 3a and 6b). On the C16 length, however, we observed stronger, longer-lasting adsorption with a different orientation driven by HB formation between the ssDNA and SAM. The ssDNA adsorbed to the C16 OH–SAM within 5 ns and remained adsorbed for the remaining 45 ns of simulation (Fig. 3b). The adsorbed conformation is primarily one with a base-down orientation, maximizing HBs to the SAM (Fig. 7b and S5b) with an average of 3.07 HBs at any given time. Interestingly, when started 40 Å away adsorption was not observed during the 100 ns MD simulations. The ssDNA moves closer to the SAM for the first 10 ns, reaching a distance of closest approach around 16Å before diffusing further way over the next 90 ns (Fig. 8a).

An interplay between hydration effects and electrostatic attractions – particularly HBs – is the probable driving force of the unpredictable ssDNA behavior on this surface observed in our study and others.[52–54] The 16Å closest-approach distance during the 40Å-starting-distance simulation supports the idea of a water hydration shell above the SAM as the cause of repulsion. This is the approximate distance water would start to feel attraction to the SAM and form more dense layers, creating an environment difficult for the ssDNA to penetrate as it would have to disrupt a greater deal of water-water and then water-SAM HBs.

To attempt to quantify water's effect, we measured the density of water within 10Å of the surface and compared that to water >20Å from the surface and found an average density of 1.01 ± 0.0250 g/cm^3 close to the surface and 0.968 ± 0.0587 g/cm^3 in the bulk water. We also found on average 0.6 water-SAM HBs per OH tail group (ESI, Fig. S7c). This indicates that approaching ssDNA would indeed have to penetrate a denser layer of water as it nears the surface. Even started just 5Å above the C11 OH–SAM, ssDNA diffuses away after ~8 ns, revealing that even if the barrier to desolvate the OH–SAM is already passed or at least significantly lessened, the water-SAM HBs were favorable enough to reform and eventually displace ssDNA. The number of DNA-SAM HBs during this 8 ns period was only 0.02 (versus 3.07 on the C16 length), showing that stable HBs could not be formed which resulted in repulsion of the DNA from the surface. The much stronger adsorption observed on the C16 length SAM is due to formation of more numerous, longer-lasting HBs than on the C11 length, possibly enabled by the higher stability of the C16 chains reflected in their slightly lower RMSD (ESI, Fig. S7a). The diffusion coefficient on the C16 OH–SAM was 2.91×10^{-7} cm^2 s^{-1} similar to the values on the COO–SAM (Table 2). Surface diffusion on the C11 length was not measured since steady adsorption was never observed.

Our results suggest that the ssDNA near the OH–SAM showed varying behavior because the lack of strong electrostatic attractions provides no long-range driving force for adsorption, however, when circumstances allow close approach of the ssDNA to the surface and formation of stable HBs, it is possible to maintain an adsorbed state.

NH–SAM From both starting distances and on both the C11 and C16 length the ssDNA was quickly adsorbed to the NH-SAM (Fig. 3a and b, 8a). Interaction energy calculations show that the clear driving force is strong electrostatic attractions to the protonated NH_3^+ tail groups (Fig. 4c and 5c). R_g stays relatively unchanged for ssDNA upon adsorption, indicating that it retains an elongated conformation on the surface due to very strong attraction of the negatively charged ssDNA backbone and HB formation with the SAM (Fig. 6c and 7c). It is interesting to note that although this SAM forms a layer of counterions like the COO–SAM (Cl^- in this case), the driving force is still the ssDNA–SAM interaction, not the ssDNA–ion interaction as was the case on the COO–SAM.

The contact map shows that the 5' cytosine and the guanine second to the 3' end are equally often the main contact point (ESI, Fig. S5). Closer inspection reveals that the negatively charged oxygens on the ssDNA backbone are oriented closest to the SAM the majority of the time, maximizing electrostatic attraction (ESI, Fig. S6c). The adsorbed ssDNA also experiences an average of 5.01 HBs at any given time, which helps to explain the frequent contact of cytosine and guanine, which both contain three HB donors or acceptors, whereas thymine and adenine contain only two.

The measured D on this SAM is by far the lowest of all at 0.203 and 0.540 × 10^{-7} cm^2 s^{-1} for the C11 and C16 SAM lengths, respectively (Table 2), over an order of magnitude lower than in bulk water and on the CH_3–SAM. Here, the ssDNA is strongly attracted to the SAM itself, specifically the protonated NH_3^+ groups, which are located randomly around the surface, creating a tendency for it to stay in regions rich in these positively charged groups. The particularly strong adsorption of ssDNA to this SAM may hinder hybridization with probes as the highly favorable surface interactions would first have to be overcome.

CH_3–SAM Starting from 5Å above the C11 length of this SAM, ssDNA is absorbed for the first 4.5 ns, desorbs for 7 ns, and then adsorbs again and remains so for the rest of the 50 ns simulation (Fig. 3a). On the C16 length, adsorption is steadier, with the ssDNA–SAM distance consistently between 2.5-5Å (Fig. 3b). The adsorption orientation is almost always end-on to the SAM i.e., the nucleotide is parallel to the SAM, which is noticeably different than on the other SAMs. Here, the adsorbed ssDNA base lies flat against the SAM in an orientation which maximizes vdW interactions (Fig. 6d and 7d). The sudden dips to more negative energies in Figure 4d around 25 and 33 ns accompany the conformational change from a single end-on contact to end-on contact by both ends (grey, Fig. 6d). Similarly, the dip in Figure 5d around 35 ns is caused by the change from single end-on contact to a conformation with two middle bases flared out, allowing them to make flush contact with the surface while the ends remain elevated (red, Fig. 7d). It's possible that adsorption of DNA to CH_3–SAM and other hydrophobic surfaces may be achieved more easily by sequences rich in adenine or guanine due to their larger surface areas and greater hydrophobicity than cytosine and thymine. Indeed, the contact map of ssDNA reveals a remarkably stable orientation with the 3' adenine consistently the closest point of contact for the majority of the simulation (ESI, Fig. S5).

From a starting distance of 40Å, the ssDNA target was never able to adsorb to the surface, despite approaching within ~4Å of the SAM at one point (Fig. 8a). From Figure 8a one can also notice the ssDNA approaches the CH_3–SAM much more closely multiple times than it did the OH–SAM, indicating again that differences in solvation effects of the SAM are important; the hydrophobic SAM appears to resist approach of the ssDNA much less than the hydrophilic one.

Diffusion on this SAM was quite fast compared to others, nearly matching that in bulk water. Elder and Jayaraman[34] also found diffusion of DNA on a hydrophobic SAM that was nearly the same as DNA in bulk water, as was our result of 8.10 and 5.93 × 10^{-7} cm^2 s^{-1} on the C11 and C16 lengths, respectively (Table 2). On the CH_3–SAM, the end-on contact is more easily maintained during sideways surface diffusion as there is less breaking and reforming of these favorable contacts than, for example, on the COO– or NH–SAMs where the strong interactions are between particular ions or charged alkanethiol chains in the SAM.

SAM Mobility

To quantify the mobility of the functionalized alkanethiol chains in each of the SAMs, we calculated the root-mean-square deviation (RMSD) for all atoms in the chains (ESI, Fig. S7a). A total of 40 chains in analogous positions in both the C11 and C16 versions of each of the SAMs were selected for measurement. We intentionally measured chains which were away from the edges of the model to avoid unrealistic edge effects and avoided measuring chains which interacted with adsorbed DNA. The OH– and COO–SAMs show a slightly smaller RMSD in the C16 length than the C11 length, while for the NH and CH_3–SAMs the two lengths are highly similar. The C16 length may experience greater stability due to the longer chain length resulting in more of the molecule being buried in the relatively stable SAM environment away from the solvent and ions. A previous study found that chain mobility increased with hydrogen bond number[25] and our findings show this same trend, with the COO–SAM having the highest RMSD and the most water–SAM HBs per tail group. The OH– and NH–SAMs where nearly identical in RMSD, despite the NH–SAM forming more HBs, and finally the CH_3–SAM showed least mobility which may be due to its inability to form HBs (ESI, Fig. S7c. We believe ions likely play a similar role to the water–SAM HBs, causing more chain movement as they interact then quickly diffuse away, which may help to explain the much higher RMSD of the COO–SAM, since the ions were very strongly adsorbed to the surface (ESI, Fig. S7b).

ssDNA Probe Dynamics on Different SAMs

A probe's conformation has important implications for use in biosensing as a linear probe will speed up hybridization kinetics relative to a curled one or one adsorbed to a surface. To quantify the dynamics of the inserted ssDNA probes, we measured the distance between the probe tip and SAM as well as the change in R_g of the probes over each 100 ns trajectory. The distance between probe tip and SAM represents the tendency of the probe to stay upright, and R_g describes a probe's tendency to change between elongated and curled conformations (a smaller R_g indicates curling). We then used principal component analysis to reveal the main modes of

probe motion over time. We also measure the electrostatic and vdW interaction energy between each probe and SAM.

Probe Tip to SAM Distances Probes remained largely upright on three of the four surfaces. Figure 9 shows snapshots from the 100 ns simulations on each of the four SAMs. The probe inserted into the COO–SAM tended to move closer to the surface over time but stopped falling around 40Å above the surface, as seen in the bumps between 40-60Å (Fig. 10a). Notably, the probe in the CH_3–SAM showed a leveling-off in the same region, moving slowly downward for the first 60 ns, then leveled off in the range 50-60Å above the SAM (Fig. 10b). Leaning of the probe past this point may result in higher-energy probe conformations as the DNA bases are forced out of their favored base stacking arrangements, but this tendency may be aided by the ability of the probes to form intramolecular HBs. Figure 11b shows intramolecular HBs for probes on the four surfaces. We can see a greater overall number of HBs for the COO– and CH_3–SAM probes compared to OH that increases slightly over time as a probe leans or curls. The probe in the OH–SAM remained well above the SAM for the entire simulation, with the tip never approaching closer than 90Å (Fig. 9a) and showed the fewest intramolecular HBs. This result is unsurprising in light of our findings in the ssDNA target simulations on the OH–SAM, in which DNA sometimes adsorbed, but other times was repelled or quickly displaced, indicating weaker overall surface interactions than the others. Hydrogen bonding was occasionally seen between the SAM and 3' end of the probe, but otherwise the probe remains in the bulk solvent where it is highly saturated by HBs and retains high mobility (Fig. 11a). In the NH–SAM, the dynamics were more straightforward and similar to the ssDNA target simulations, as the probe was immediately attracted strongly to the surface and fell completely onto the SAM within 5 ns where it remained strongly adsorbed for the rest of the simulation (Fig. 9c and 10c). Considering the dynamics of all different surfaces except the NH–SAM, in the absence of any strong surface attractions probes appear to stay upright, tending to occupy the bulk solvent where they engage highly in DNA–water HBs and retain a great deal of mobility.

Probe Radius of Gyration and Principal Components of Motion Our results show a general trend of a shrinking R_g as probes move closer to a SAM, which we attribute to movement of the probe from the more isotropic bulk water environment to the anisotropic surface which causes it to change conformation to maximize favorable surface interactions. This trend is easily visible on the COO– and CH_3–SAMs (Fig. 10). On the COO–SAM, the plot of R_g traces a very similar shape to the probe-SAM distance plot: both show peaks in the beginning as repulsion from the SAM (and therefore distance) is greatest, then a general downtrend and leveling-off after about 60 ns. The degree of probe curling is not very high in contrast to the ssDNA target on this SAM, likely due to the anchoring of one end of the probe to the gold substrate. The dynamics on the CH_3–SAM overall were quite similar to that on the COO–SAM as can be seen in Figure 10, with a shrinking R_g as the probe approaches the surface driven by increasing intramolecular HBs and shifting of the 3' end of the probe to maximize vdW interactions with the hydrophobic SAM. On the OH–SAM, there was a small degree of probe curling indicated by R_g fluctuating smoothly between 24-30Å, which is probably a natural degree of fluctuation as the others showed roughly this same pattern. Since the probe never really approached the surface, no systematic downtrend was

observed, and overall R_g on this SAM was the most unchanged, reflecting the results in the previous sections which suggest ssDNA probes are quite stable on the OH–SAM. On the NH–SAM, the rapidly shrinking R_g as the probe is strongly attracted and adsorbs to the SAM indicates that it does so in a highly curled conformation as it is forced into the favored backbone-down conformation that maximizes attraction to the positively charged surface. (Fig. 10b).

The principal components of probe motion gathered from our PCA analysis showed motions both shared and unique among probes on various SAMs (Fig. 12). The linker molecule that bonds the probes to the gold extends slightly above the SAM before connecting to the 3' end and allows the probe to rotate readily, yielding one of the main motions observed (ESI, Fig. S8). Probes on the COO–, OH–, and CH_3–SAMs all exhibited rotation around the linker. A more dominant motion on the COO–SAM was an elongation accompanied by uncoiling, probably due to the initial repulsion from the SAM before the Na^+ layer formed. This motion is also evident in the increase in probe tip-SAM distance in the beginning of the plot in Figure 10a. This same motion was seen to a lesser degree on the OH– and CH_3–SAMs, and accounts for the small recurrent fluctuation of R_g displayed by all the probes (except on the NH–SAM). Finally, a common motion in all probes was a downward curling, especially of the top five or six bases, as the DNA interacts and forms intramolecular HBs.

Probe-SAM Interaction Energies The probe on the COO–SAM, as in the ssDNA target simulations on this surface, was repelled initially but began to feel attraction to the surface after a positive ionic layer formed at the SAM–water interface. Although the sequence of the probe is different (complimentary) than the targets, the negative charges on the backbone remain, so this interaction is largely unchanged. However, unlike the ssDNA target, the probe never adsorbed to the SAM despite leaning downward significantly. From Figure 13a, we can see that the total interaction with the SAM plus ions is highest in the beginning then levels off. This is due to the attraction of the probe to ions in solution, but as more and more ions adsorb to the surface, the interaction diminishes since the probe remains upright. The probe on the OH–SAM had relatively surface interaction, experiencing short-lived HBs and vdW interactions between the 3' end of the probe or its linker molecule and the SAM (Fig. 13b). Even though hydrogen bonding between the probe and the OH–SAM is possible, it offers little increase in stability as the probe already forms many HBs with the surrounding water. Interaction energy calculations on the CH_3–SAM show that vdW forces are the dominant ones, showing very similar strength to those on the OH–SAM arising from the 3' thymine and linker molecule interacting with the SAM (Fig. 13d). The absence of any other strong surface attractions causes this probe to stay largely upright where it can maximize DNA-water HBs while retaining high mobility.

The probe adsorbed very rapidly to the NH-SAM, clearly driven by strong electrostatic attraction to the positively charged NH_3^+ tail groups (Fig. 13c). Therefore DNA interaction with this SAM will be highly pH– and salt concentration–dependent, and the number of protonated (positively charged) tail groups drives the interaction. However, if enough counter ions are present to associate with the charged groups, DNA behavior near this surface may potentially be altered by a counter ion effect similar to the one observed on the COO-SAM. Overall, the dynamics of ssDNA

probes on the NH–SAM are highly similar to that of ssDNA targets due to dominant electrostatic attractions between the DNA backbone and positively charged functional groups of the SAM. In fact, we also see here the backbone-down orientation of the probe after adsorption (Fig. 9c).

Interaction Between Nearby ssDNA Probes

Interaction between nearby probes on a sensor surface may induce conformational changes that affect hybridization kinetics.[56] Previous experimental studies have shown significant heterogeneity in probe surface concentration, resulting in widely varying nearest-neighbor-distances which could be as small as a few tens of Angstroms.[21,55] These simulations used two probes inserted into the OH-SAM. The probe is approximately 120Å in length, so scenarios were tested up to a distance where probes had a reasonable chance of leaning into contact with one another. To measure the effect of varying inter-probe distance, we calculate the distance between the probe tips and SAM and the probes' radii of gyration, as well as the probe-probe interaction energy for two probes either 25, 50, or 100Å apart.

Repulsion of Nearby Probes Induces Conformational Changes At a separation distance of 25Å, the probes showed clear repulsion and marked changes in orientation with respect to the surface (Fig. 14). Figure 15b shows the strong repulsion between probes due to the high negative charges of the two molecules. Such strong repulsion results in much closer approach of the probes to the SAM surface over time, pushing one of the probes in the simulation to within ~43Å (Fig. 15a). The other probe was much more upright, remaining between 100-120Å above surface for most of the simulation before falling to around 80Å. At a 50Å separation distance, although probes still repel one another, the difference in orientation compared to an isolated probe is much less pronounced. In this case, one of the probes is between 60-80Å above the SAM during the latter 25 ns of simulation while the other is steadily between 80-90Å, similar to an isolated probe on this SAM (Fig. 15a). Surprisingly, in both the 25 and 50Å separation cases, R_g does not show the typical downtrend, even as probes approach the surface much more closely than in isolated cases (Fig. 15c). This could be a result of dominant probe-probe repulsion forcing probes into a straighter conformation that maximizes inter-probe distance. At a separation of 100Å, probe dynamics are essentially the same as for isolated probes. In both the 25 and 50Å separation scenarios probes approached the SAM more closely than an isolated probe. Such a difference in orientation may be even more pronounced on SAMs which more strongly attract DNA, since nearby probes clearly repel one another toward the surface. In such cases, the probe is more likely to adsorb to the surface if possible, altering hybridization kinetics with incoming targets by becoming sterically hindered and raising the energy barrier to hybridization. Conversely, a SAM which repels probes may suffer less from the effects we observed, as the repulsive forces may counteract changes induced by nearby probes. It's clear from our results that nearby probes induce changes in probe orientation and conformation that need to be considered as these factors will undoubtedly affect hybridization.

Conclusions

We studied the behavior of ssDNA targets near hydrophobic, hydrophilic, and oppositely charged surfaces to measure the effect of greatly varying surface properties on their behavior and to understand the implications of this behavior for nucleic acid biosensing. We also studied the behavior of 29-base linear ssDNA probes inserted into these surfaces to answer questions about their dynamics on various surfaces and interactions with other nearby probes, both having major influence on DNA hybridization kinetics and the rational design of biosensors.

Simulations of ssDNA targets on a COO-SAM revealed that the DNA is strongly repelled by the charged COO^- tail groups but was able to associate with the layer of Na^+ ions that formed on the surface after several nanoseconds. This result shows that ions in solution can adsorb on a surface and drive DNA behavior, affecting both adsorption tendency and diffusivity, and it highlights the importance of the ionic strength of solutions and the role of ions in intermolecular interactions, especially near charged surfaces. ssDNA target simulations on the OH–SAM showed varying behavior due to an interplay between hydration of the hydrophilic surface and hydrogen bonding between the ssDNA and SAM. We conclude that a dense hydration layer repels DNA and competes with intermolecular ssDNA–SAM HBs based on our measurement of higher water density near the SAM than in bulk water. However, when the ssDNA was started 5Å from this SAM, we observed steady adsorption driven by HBs and vdW forces on the C16 length. ssDNA was strongly attracted to the NH-SAM by the protonated NH_3^+ tail groups, yielding much slower diffusion and indicating that DNA behavior on this SAM depended highly on its protonation state and the ionic strength of the solution. Interestingly, despite a strong counterion presence here, behavior was driven by ssDNA–SAM interactions, unlike in the case of the COO–SAM. On the hydrophobic CH_3–SAM, ssDNA adsorbed in an end-on orientation maximizing vdW forces when started just 5Å away but did not adsorb when started 40 Å away due to a lack of long-range forces to drive adsorption.

Probe dynamics and orientation on a surface strongly influence the rate and probability of hybridization with incoming targets, so understanding their behavior is essential. On the COO–SAM, the probe was strongly repelled from the surface but was attracted to the positive ionic layer on top of the surface. It remained upright in the bulk solvent for the entire simulation, showing just a slight tendency to lean and curl, which was driven at least in part by the formation of intramolecular HBs. On the OH–SAM, the ssDNA probe was remarkably stable, remaining upright to a larger degree than in other cases, and showed very little tendency to curl, which seemed to generally increase as a probe moved closer to a surface. We attribute the probe behavior here to the same factors as in the ssDNA target simulation: there is a dense hydration layer above the SAM repelling the probe and a lack of strong long-range DNA–SAM electrostatic attraction. On the NH–SAM, probe behavior was straightforward: it immediately felt strong attraction to the positive charges and was completely adsorbed to the surface, where it remained for the final 80 ns of simulation. The probe was highly immobile on the surface due to the strong attraction of the negatively charged DNA backbone to positively charged tail groups in the SAM. On the CH_3–SAM the probe showed relatively high stability, similar to the OH–SAM. It stayed elevated at least 50Å above the surface for the entire 100 ns. We found that the main DNA–SAM interactions on this surface arose from vdW forces in an end-on orientation of DNA, requiring a very close approach to the surface. Such an orientation may be difficult for a probe to achieve

since one end is bonded to the gold substrate and saturation of the other is saturated by HBs with the bulk water, making upright orientations more favorable.

The multiple-probe simulations showed that at close range probes exert significant influence on one another. Namely, the probes repel one another strongly at separation distances around 25Å and move closer to the SAM surface. At 50Å, repulsion is reduced but still induced orientations closer to the surface than in isolated probe scenarios, and probes separated by 100Å showed no difference from isolated ones. Additionally, nearby probes showed a very interesting tendency not to curl as much as isolated ones, likely because of the strong repulsive forces driving them to maximize inter-probe distance. The main implication of our multiple-probe simulations is that high probe surface density will almost certainly affect hybridization rates through a combination of factors that influence probe conformation and orientation with respect to the surface. The magnitude of the effect will vary depending on the probe surface density and the surface type. SAMs that attract DNA may exaggerate this effect and be more likely to experience probe adsorption, whereas SAMs which repel DNA may somewhat mitigate such effects.

Conflicts of Interest

There are no conflicts to declare.

Acknowledgements

The research reported in this publication was supported by US National Science Foundation (MCB-1350401) and NSF national supercomputer centers (TG-CHE130009). We thank Dr. Tao Ye and Qufei Gu for discussions relating to the DNA probe and SAM systems studied here, Drs. Dormidontova and Dahal for discussion regarding MD simulation of gold atoms, and Dr. Chris Roberts for development of in-house programs to expedite the modeling process.

References

1. J. I. A. Rashid, N. A. Yusof, *Sensing and Bio-Sensing Research*, 2017, **16**, 19
2. E. E. Ferapontova, *Annual Review of Analytical Chemistry*, 2018, **11**, 197.
3. Y. Zhou, L. Tang, G. Zeng, C. Zhang, Y. Zhang, X. Xie, *Sensors and Actuators B: Chemical*, 2016, **223**, 280.
4. T. G. Drummond, M. G. Hill and J. K. Barton, *Nature biotechnology*, 2003, **21**, 1192.
5. J. Zhang, L-L. Wang, M-F. Hou, Y-K. Xia, W-H. He, A. Yan, Y-P. Weng, L-P. Zeng, J-H. Chen, *Biosensors and Bioelectronics*, 2018, **102**, 33.
6. Q. Gu, W. Nanney, H. H. Cao, H. Wang and T. Ye, *Journal of the American Chemical Society*, 2018, **140,** 14134.
7. X. Hao, E. A. Josephs, Q. Gu and T. Ye, *Nanoscale*, 2017, **9**, 13419.
8. G. R. Abel, E. A. Josephs, N. Luong, T. Ye, *Journal of the American Chemical Society*, 2013, **135**, 6399.

9. M. Jarczewska, E. Kierzkowska, R. Ziółkowski, Ł. Górski, E. Malinowska, *Bioelectrochemistry*, 2015, **101**, 35.
10. M. Lin, P. Song, G. Zhou, X. Zuo, A. Aldalbahi, X. Lou, J. Shi, and C. Fan, *Nature Protocols*, 2015, **11**, 1244.
11. K. L. Prime and G. M. Whitesides, *Journal of the American Chemical Society*, 1993, **115**, 10714.
12. C. Fan, K. W. Plaxco and A. J. Heeger, *Proceedings of the National Academy of Sciences*, 2003, **100**, 9134.
13. A. Sassolas, L. J. Blum and B. D. Leca-Bouvier, *Biotechnology Advances,* 2012, **30**, 489.
14. N. Arroyo-Curras, J. Somerson, P. A. Vieira, K. L. Ploense, T. E. Kippin and K. W. Plaxco, *Proceedings of the National Academy of Sciences*, 2017, **114**, 645.
15. M.T. Cygan, G.E. Collins, T.D. Dunbar, D.L. Allara, C. G. Gibbs and C. D. Gutsche, *Analytical Chemistry*, 1999, **71**, 142.
16. S.Y. Park, J.S. Lee, D. Georganopoulou, C.A. Mirkin and G.C. Schatz, *Journal of Physical Chemistry B*, 2006, **110**, 12673.
17. H. Noh, A.M. Hung and J.N. Cha, *Small*, 2011, **7**, 3021.
18. A. Seifpour, S.R. Dahl, B. Lin and A. Jayaraman, *Molecular Simulation*, 2013, **39**, 741.
19. T. M. Herne and M. J. Tarlov, *Journal of the American Chemical Society*, 1997, **119**, 8916.
20. A. B. Steel, T. M. Herne and M. J. Tarlov, *Analytical chemistry*, 1998, **70**, 4670.
21. E. A. Josephs and T. Ye, *ACS nano*, 2013, **7**, 3653.
22. X. L. Luo and J. J. Davis, *Chem. Soc. Rev*, 2013, **42**, 5944.
23. B. Park, M. Chandross, M. J. Stevens and G. S. Grest, *Langmuir*, 2003, **19**, 9239.
24. J. Zheng, L. Li, S. Chen and S. Jiang, *Langmuir*, 2004, **20**, 8931.
25. A. J. Pertsin and M. Grunze, *Langmuir*, 2000, **16**, 8829.
26. U. R. Dahal, Z. Wang and E. E. Dormidontova, *Macromolecules*, 2017, **50**, 6722.
27. S. S. Jang, Y. H. Jang, Y. H. Kim, W. A. Goddard, A. H. Flood, B. W. Laursen and D. W. Steuerman, *Journal of the American Chemical Society*, 2005, **127**, 1563.
28. L. Li, S. Chen, J. Zheng, B. D. Ratner and S. Jiang, *The Journal of Physical Chemistry B*, 2005, **109**, 2934.
29. J. Zheng, L. Li, H. K. Tsao, Y. J. Sheng, S. Chen and S. Jiang, *Biophysical journal*, 2005, **89**, 158.
30. L. Li, S. Chen, J. Zheng, B. D. Ratner and S. Jiang, *The Journal of Physical Chemistry B*, 2005, **109**, 2934.
31. J. Liu, G. Yu and J. Zhou, *Chemical Engineering Science*, 2015, **121**, 331.
32. N. Schwierz, D. Horinek, S. Liese, T. Pirzer, B. N. Balzer, T. T. Hugel and R. R. Netz, *Journal of the American Chemical Society*, 2012, **134**, 19628.
33. J. H. Park and N. R. Aluru, *Applied Physics Letters,* 2010, **96,** 123703.
34. R. M. Elder and A. Jayaraman, *Soft Matter*, 2013, **9**, 11521.
35. S. Wang, S. Dai and D. E. Jiang, *ACS Applied Nano Materials*, 2018, **2**, 379.
36. D. J. Graves, *Trends in biotechnology*, 1999, **17**, 127.
37. M. Schena, R. A. Heller, T. P. Theriault, K. Konrad, E. Lachenmeier and R. W. Davis, *Trends in biotechnology*, 1998, **16**, 301.
38. R. A. Sheldon, *Advanced Synthesis and Catalysis*, 2007, **349**, 1289.

39. S.O. Kelley, C.A. Mirkin, D.R. Walt, R.F. Ismagilov, M. Toner and E.H. Sargent, *Nature Nanotechnology*, 2014, **9**, 969.
40. P. Gong and R. Levicky, *Proceedings of the National Academy of Sciences*, 2008, **105**, 5301
41. D. Irving, P. Gong and R. Levicky, *The Journal of Physical Chemistry B*, 2010, **114**, 7631.
42. F. Schreiber, *Progress in surface science*, 2000, **65**, 151.
43. M.T. Nelson, W. Humphrey, A. Gursoy, A. Dalke, L.V. Kalé, R.D. Skeel and K. Schulten, *International Journal of of High Performance Computing Applications,* 1996, **10**, 251.
44. J.A. Maier, C. Martinez, K. Kasavajhala, L. Wickstrom, K.E. Hauser and C. Simmerling, *Journal of Chemical Theory and Computation*, 2015, ***11,*** 3696
45. J. Wang, R.M. Wolf, J.W. Caldwell, P.A. Kollman and D.A. Case, *Journal of Computational Chemistry*, 2004, **25**, 1157.
46. A. Jakalian, B. L. Bush, D. B. Jack and C. I. Bayly, *Journal of computational chemistry*, 2000, **21**, 132.
47. B. Hess, C. Kutzner, D. van der Spoel and E. Lindahl, GROMACS 4: Algorithms for Highly Efficient, Load-Balanced, and Scalable Molecular Simulation, *Journal of Chemical Theory and Compuation*, 2008, **4**, 435.
48. W. Humphrey, A. Dalke and K. Schulten, *Journal of Molecular Graphics*, 1996, **14**, 33.
49. J.E. Stone, An Efficient Library for Parallel Ray Tracing and Animation, University of Missouri, Rolla, 1998.
50. H. Hotelling, *Journal of Educational Psychology*, 1933, **24**, 417.
51. J. H. Monserud and D. K. Schwartz, *Biomacromolecules*, 2012, **13**, 4002.
52. J. C Hower, Y. He and S. Jiang, *The Journal of chemical physics*, 2008, **129**, 12B601.
53. N. Schwierz, D. Horinek, S. Liese, T. Pirzer, B. N. Balzer, T. Hugel and R. R. Netz, *Journal of the American Chemical Society*, 2012, **134**, 19628.
54. M. Kastantin and D.K. Schwartz, *Small*, 2012, **9**, 933.
55. A. W. Peterson, R. J. Heaton and R. M. Georgiadis, *Nucleic acids research*, 2001, **29**, 5163.

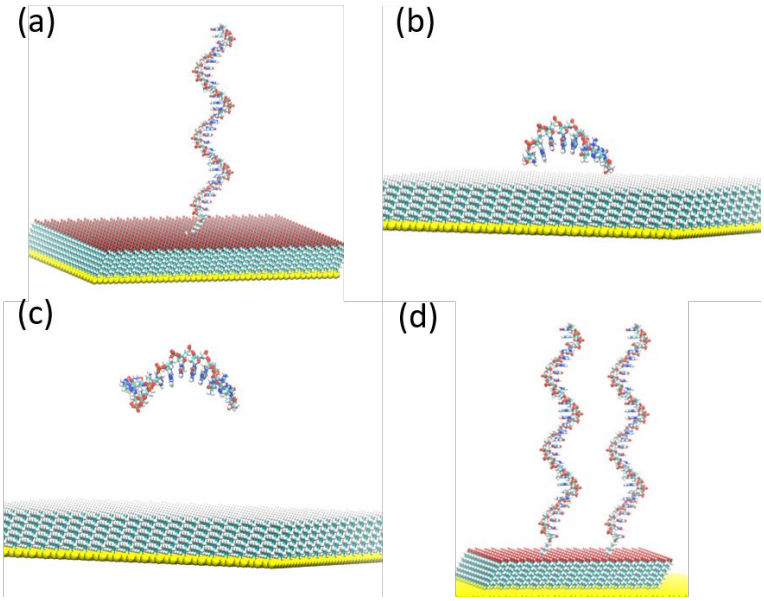

Figure 1. Simulation models of a) a ssDNA probe inserted into a SAM, a ssDNA target started b) 5 Å or c) 40 Å above a SAM, and d) a multiple-probe simulation with two probes separated by 25Å.

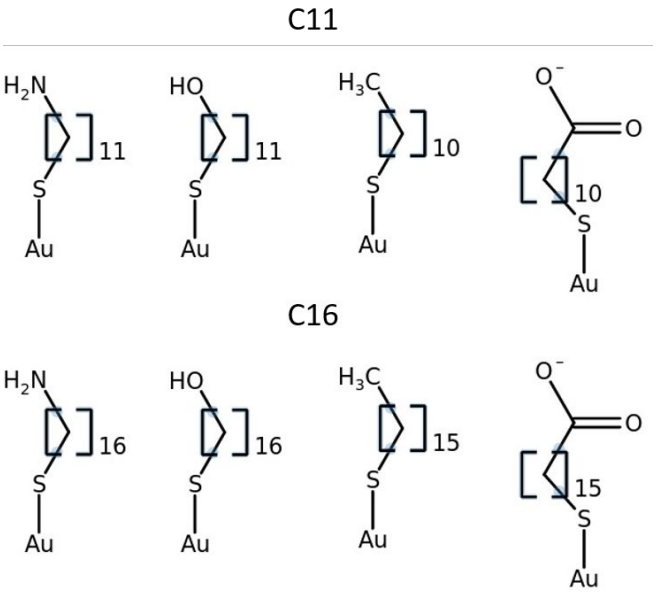

Figure 2. Chemical structures of the two different lengths of functionalized alkanethiols used in the SAMs.

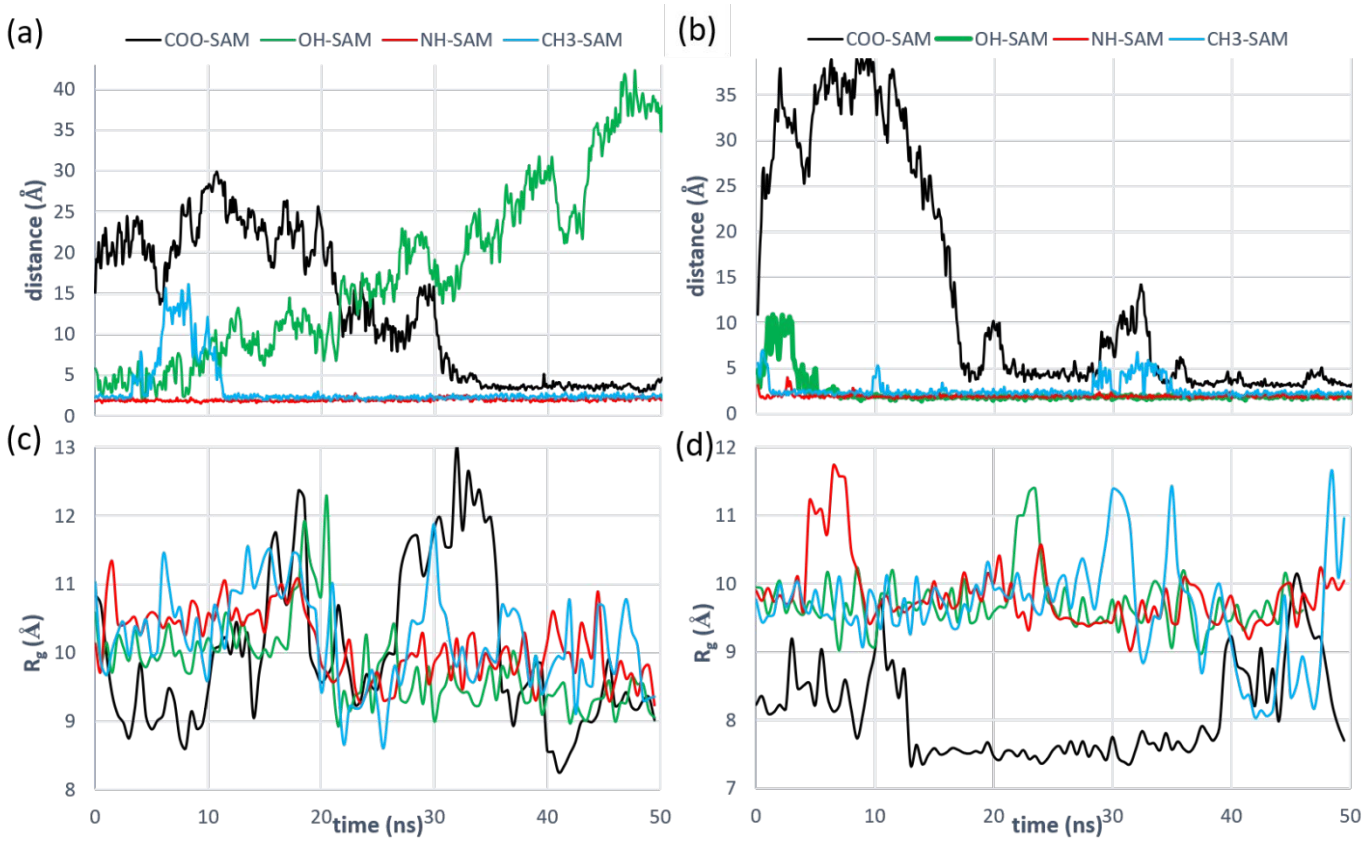

Figure 3. Minimum distance between the ssDNA target and SAM from the 5Å starting distance for a) the C11 and b) C16 length, and radius of gyration of the ssDNA targets during the same simulation for the c) C11 and d) C16 length SAMs.

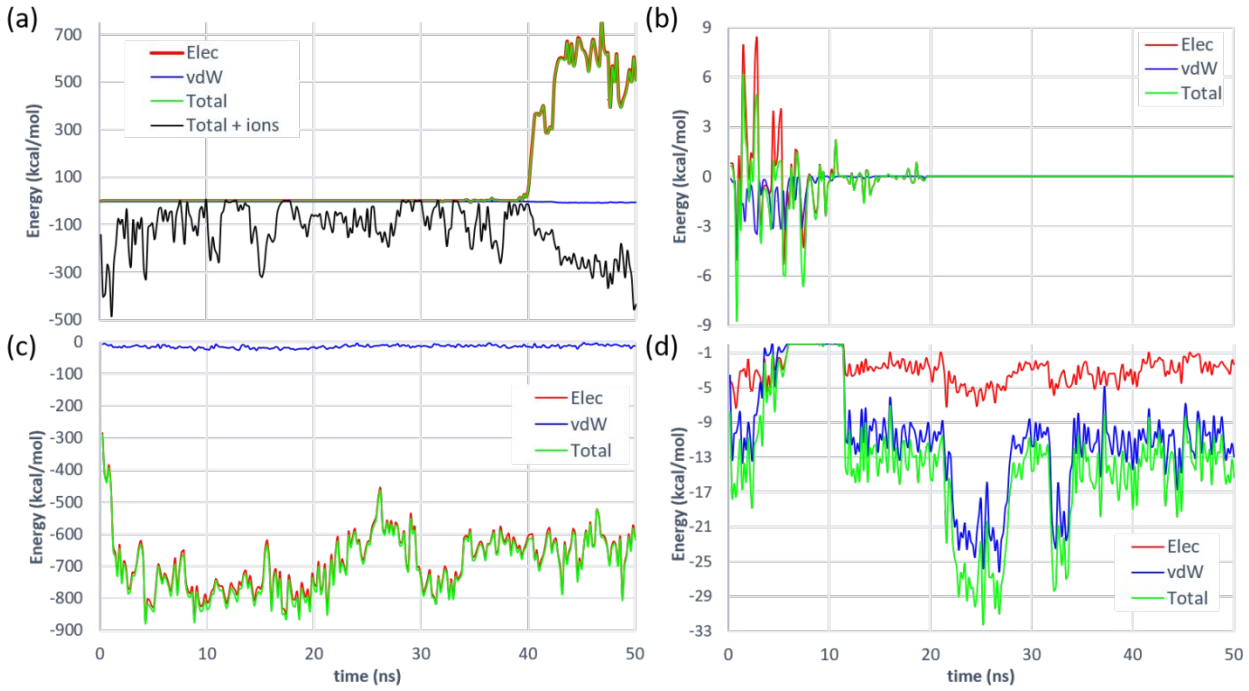

Figure 4. Plots of the electrostatic (Elec) and vdW interaction energy and their sum (Total) between the 8-base ssDNA target and the entire SAM when started 5 Å above the C11 length of a) the COO-SAM, b) the OH-SAM, c) the NH-SAM, and d) the CH_3-SAM. In (a), "Total + ions" is the sum of Elec, vdW, and the electrostatic interaction of the ssDNA with the Na+ ions.

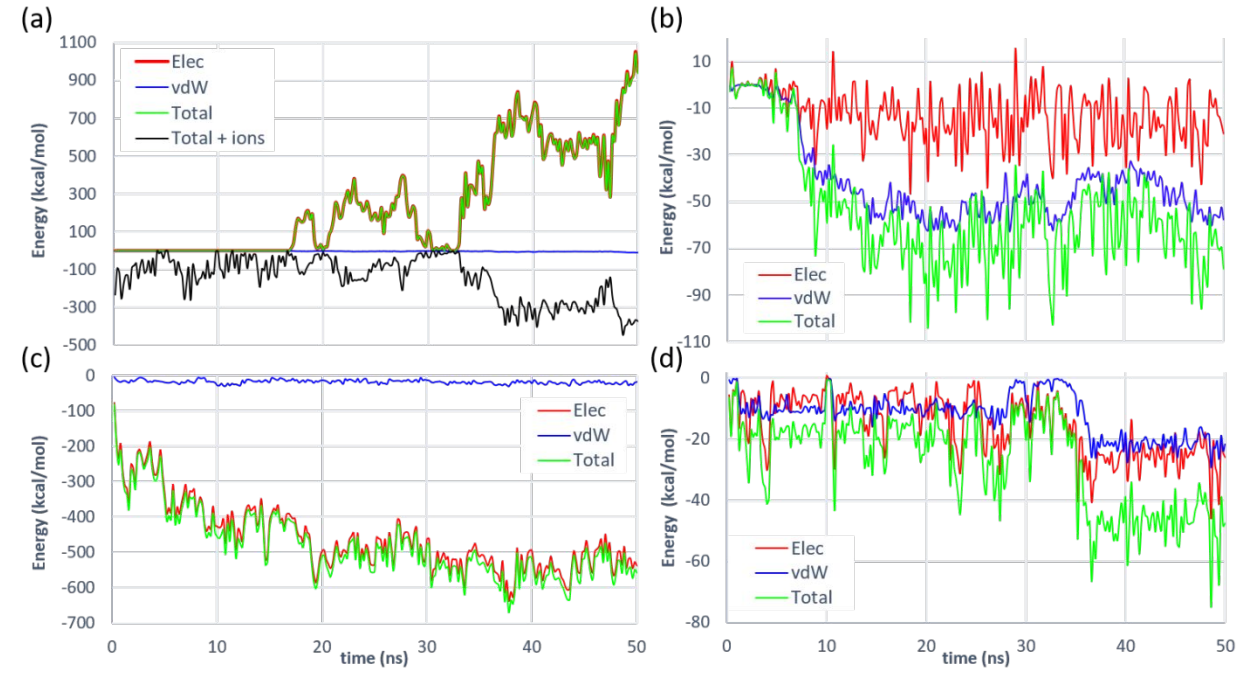

Figure 5. Plots of the electrostatic (Elec) and vdW interaction energy and their sum (Total) between the 8-base ssDNA target and the entire SAM when started 5 Å above the C16 length of a) the COO-SAM, b) the OH-SAM, c) the NH-SAM, and d) the CH_3-SAM. In (a), "Total + ions" is the sum of Elec, vdW, and the electrostatic interaction of the ssDNA with the Na+ ions.

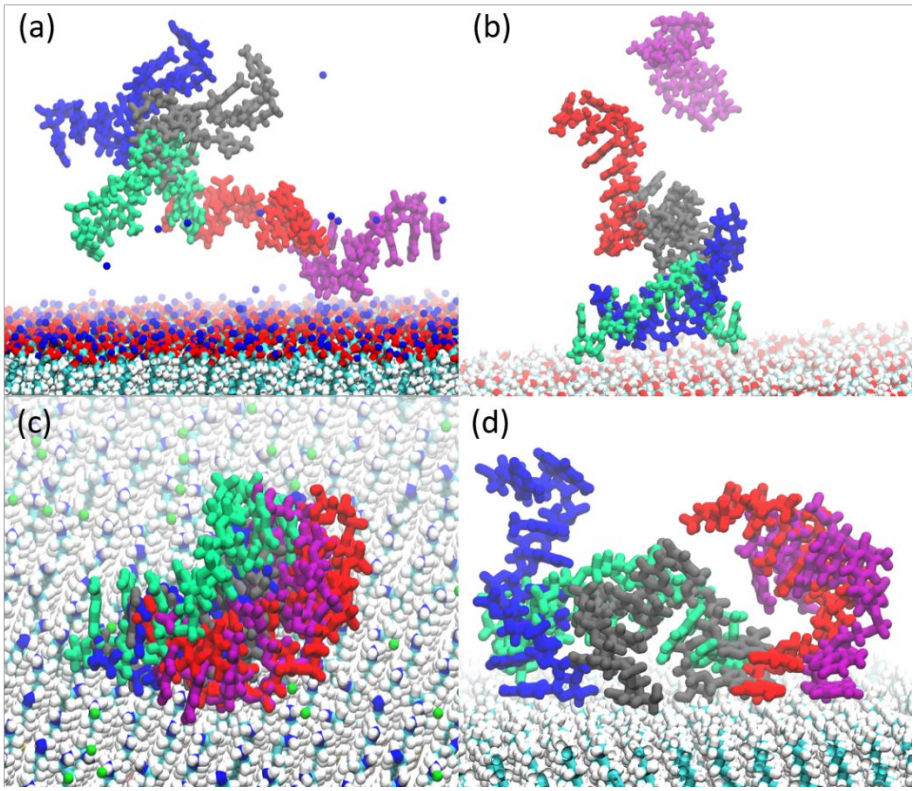

Figure 6. Snapshots from the 50 ns simulations of an 8-base ssDNA target started 5 Å above the C11 length of a) the COO-SAM (Na^+ ions shown as blue spheres), b) the OH-SAM, c) the NH-SAM (Cl^- ions shown as green spheres), and d) the CH_3-SAM. Snapshots are shown at 0 ns (green) and every ~12.5 ns thereafter in the order: blue, grey, red, and finally purple. The ssDNA shifts slightly during equilibration, so the green snapshots appear oriented differently even though all are taken at 0 ns of production MD.

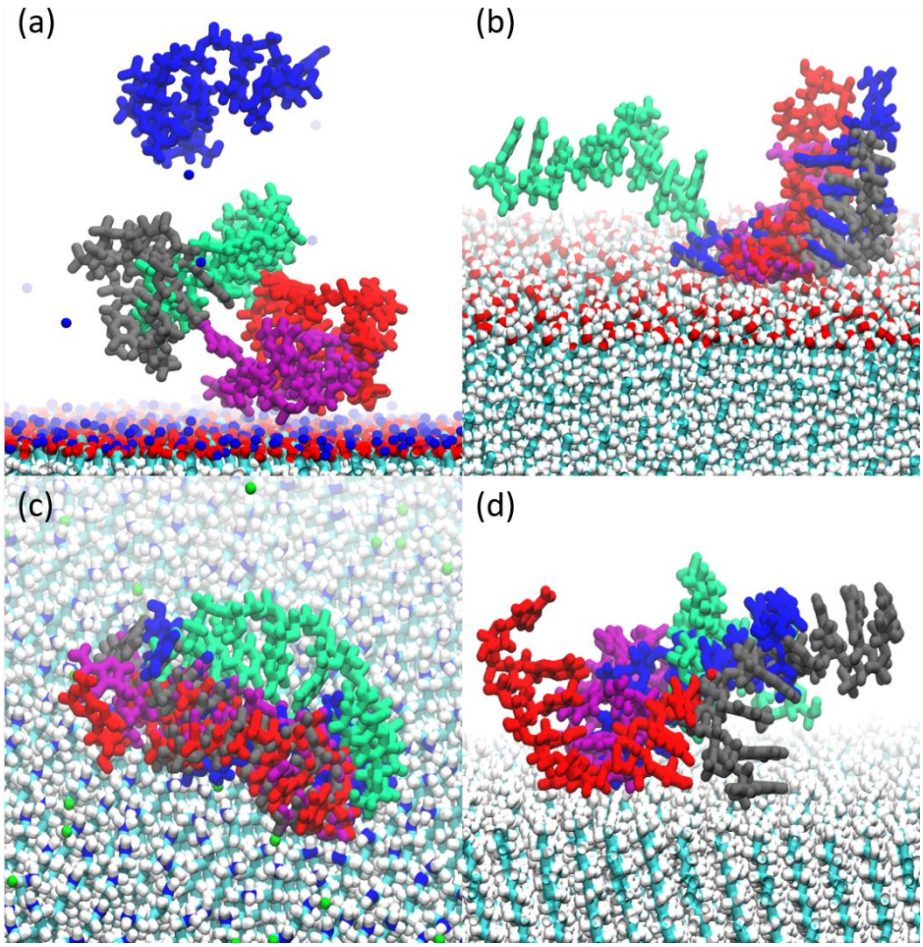

Figure 7. Snapshots from the 50 ns simulations of an 8-base ssDNA target started 5 Å above the C16 length of a) the COO-SAM (Na^+ ions shown as blue spheres), b) the OH-SAM, c) the NH-SAM (Cl^- ions shown as green spheres), and d) the CH_3-SAM. Snapshots are shown at 0 ns (green) and every ~12.5 ns thereafter in the order: blue, grey, red, and finally purple.

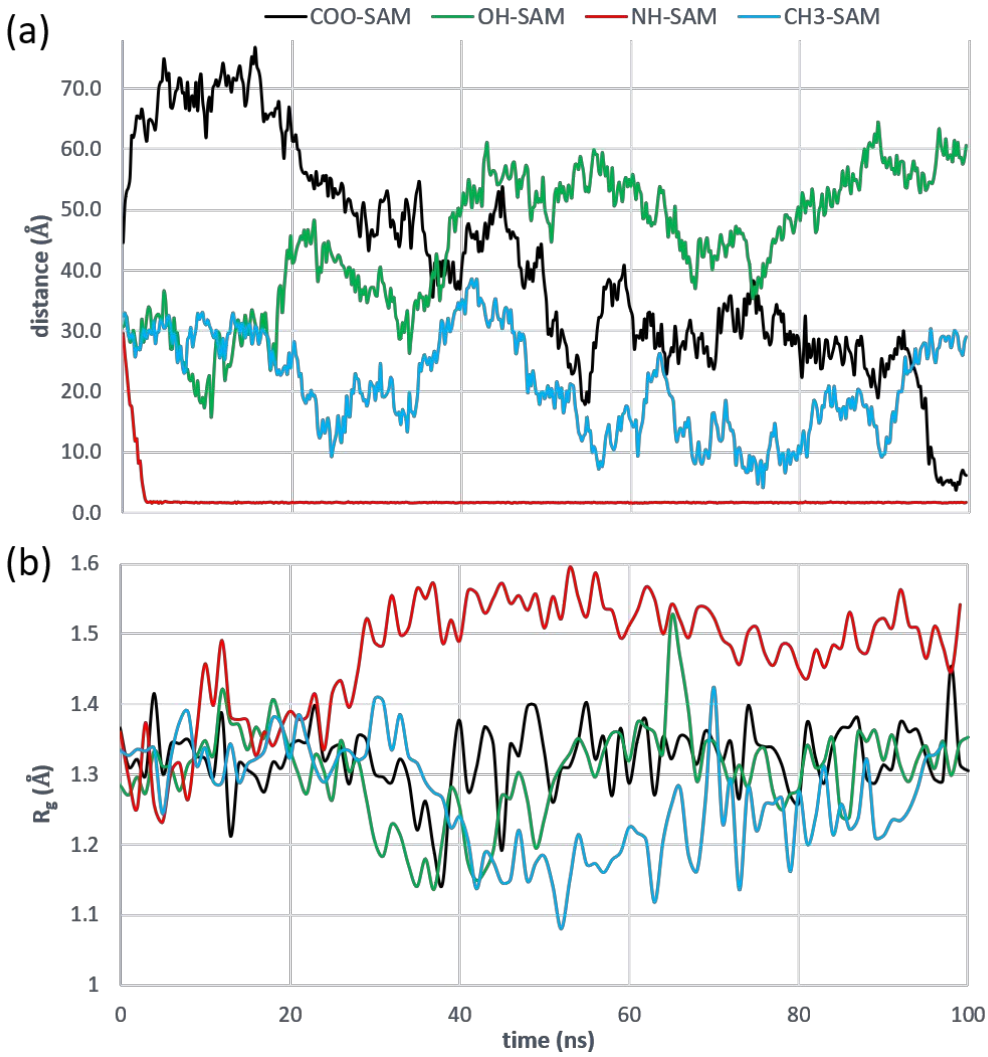

Figure 8. a) minimum distance from DNA to SAM during simulations with 40Å DNA-SAM starting distance and b) the ssDNA radius of gyration for each SAM during the same simulation.

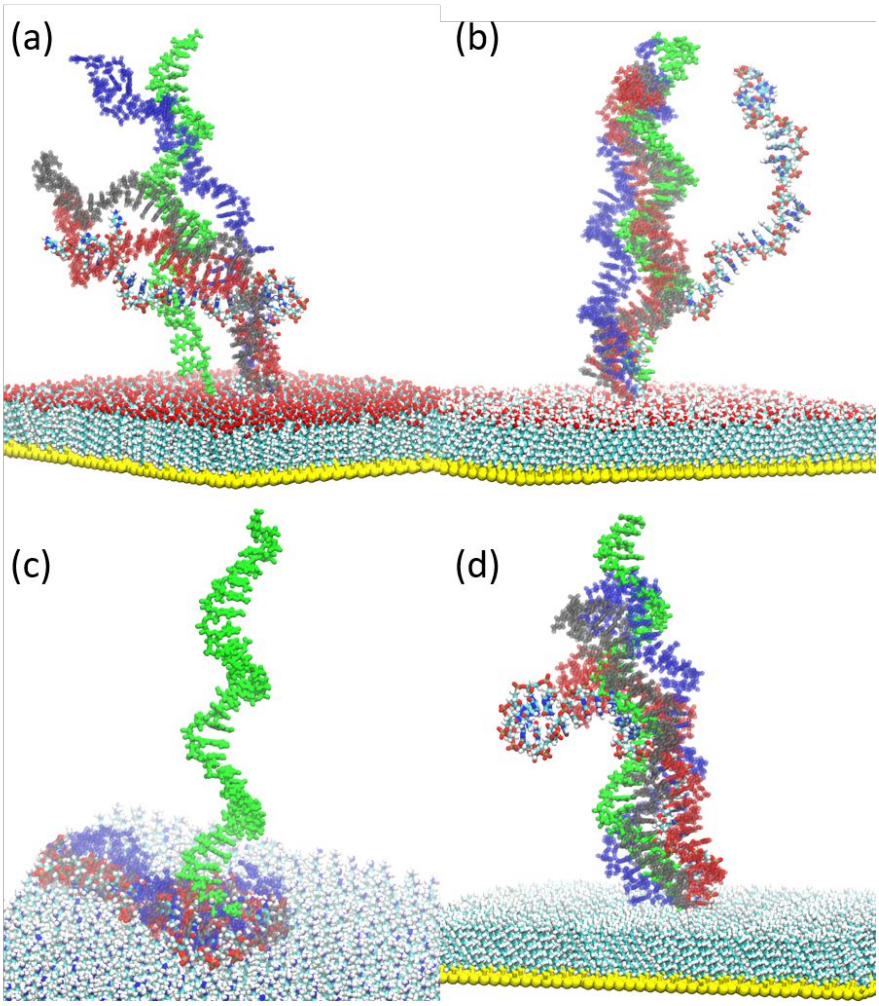

Figure 9. Snapshots from the 100 ns probe simulations in a) the COO-SAM, b) the OH-SAM, c) the NH-SAM, and d) the CH_3-SAM. Snapshots are shown at 0 ns (green) and every ~25 ns thereafter in the order: blue, grey, red, and finally multi-color.

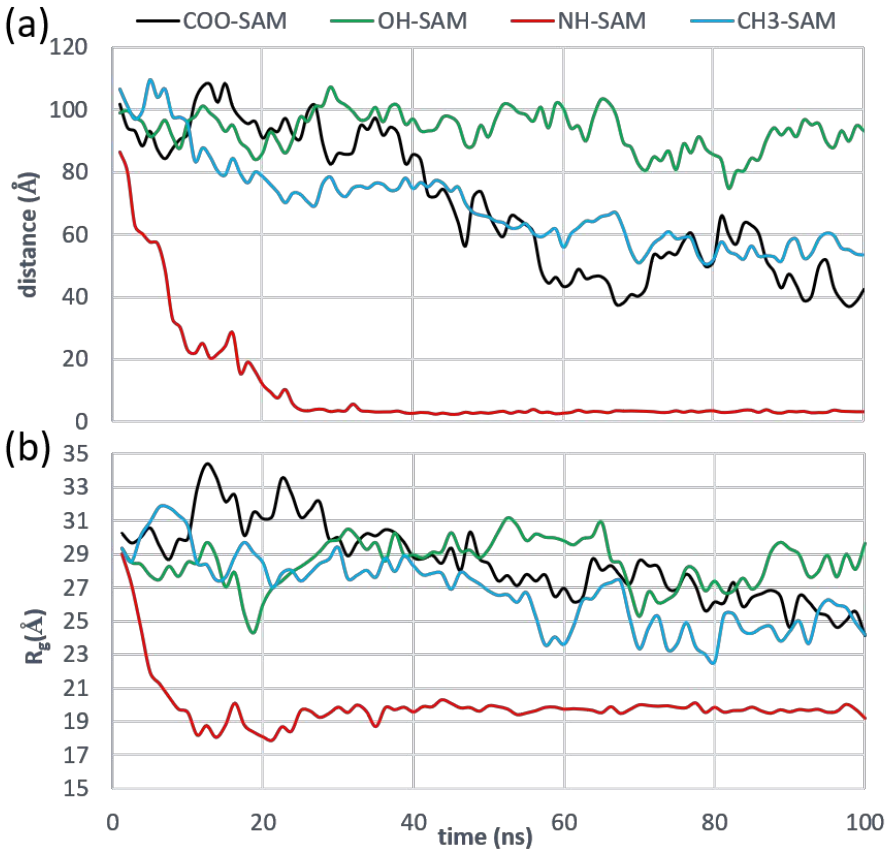

Figure 10 a) distance from probe tip to SAM and b) probe radius of gyration over the 100 ns trajectories. The plots of distance and R_g are remarkably similar, as R_g rises and falls in step with distance.

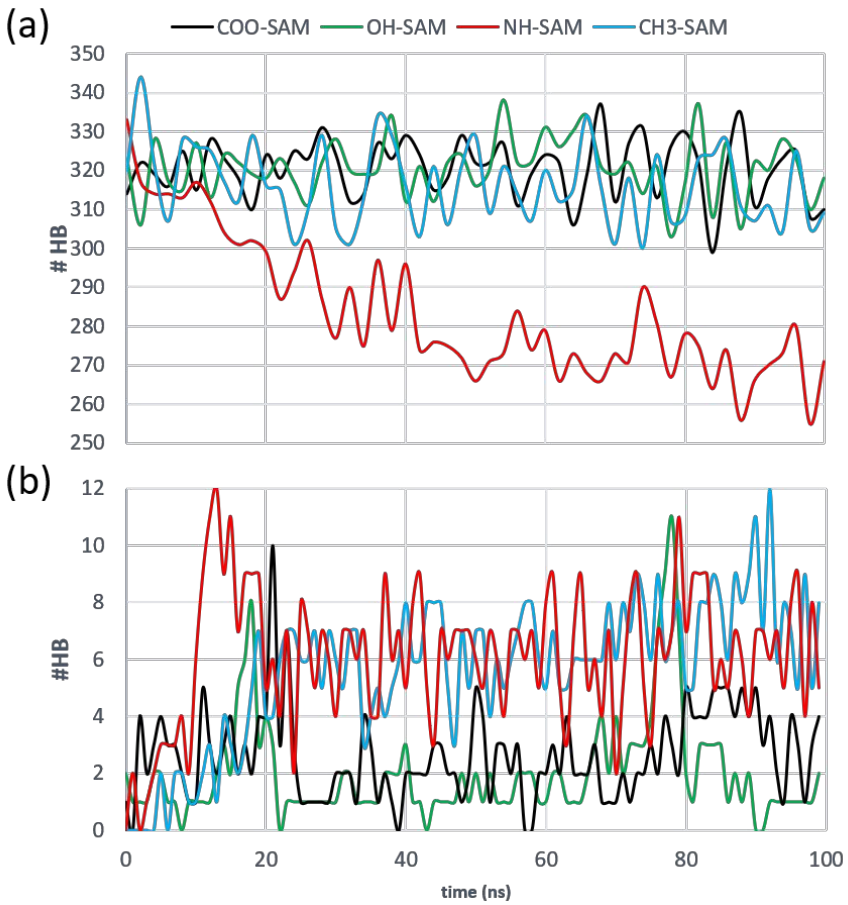

Figure 11. a) probe-water HBs and b) probe intramolecular HBs during the 100 ns trajectories. Intramolecular HBs increase over time as probes lean and become more curled.

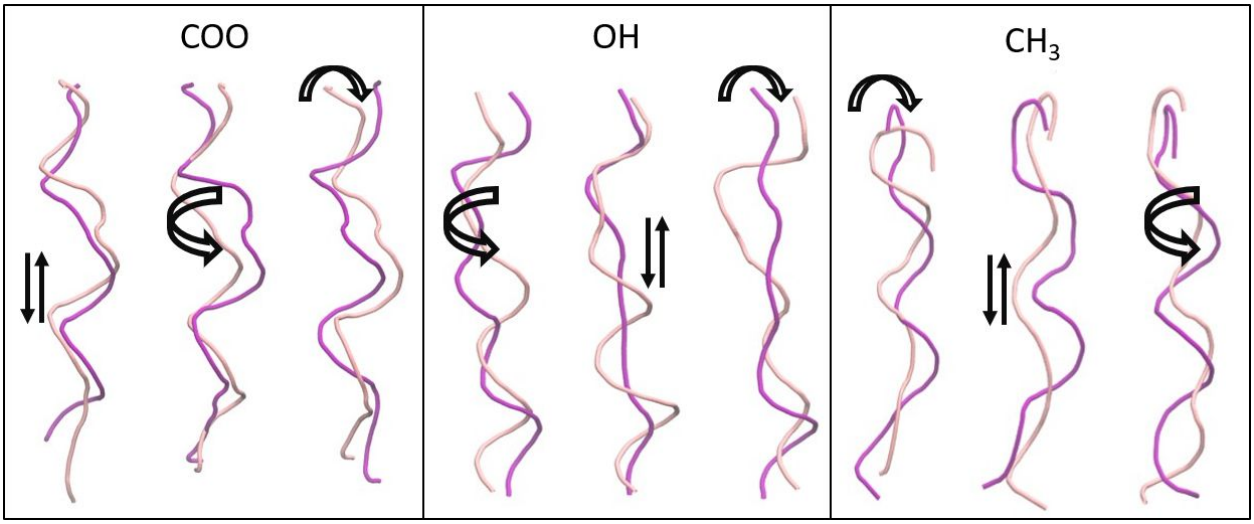

Figure 12. Principal components of probe motion on different SAMs. The first three PC modes are shown from left to right in order of decreasing contribution to the overall probe mobility. NH-SAM probe not shown since it adsorbed rapidly.

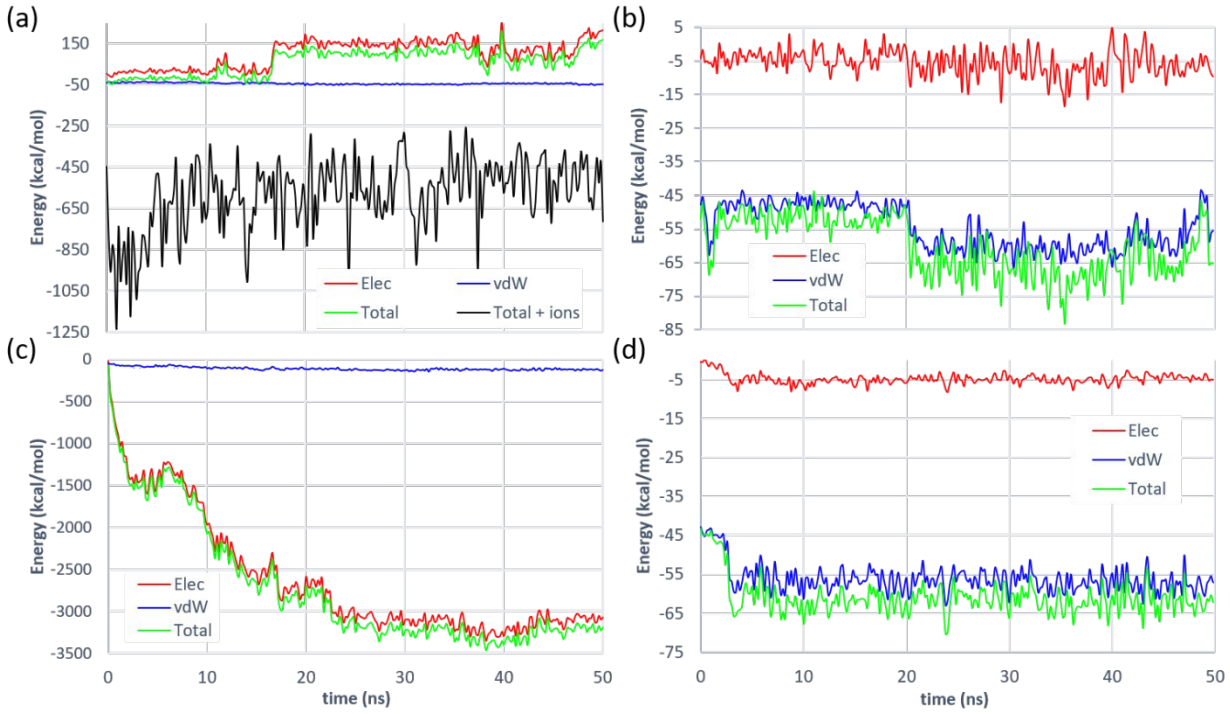

Figure 13. Plots of the electrostatic (Elec) and vdW interaction energy and their sum (Total) between the ssDNA probe and the entire SAM in a) the COO-SAM, b) the OH-SAM, c) the NH-SAM, and d) the CH_3-SAM. In (a), "Total + ions" is the sum of Elec, vdW, and the electrostatic interaction of the probe with the Na+ ions.

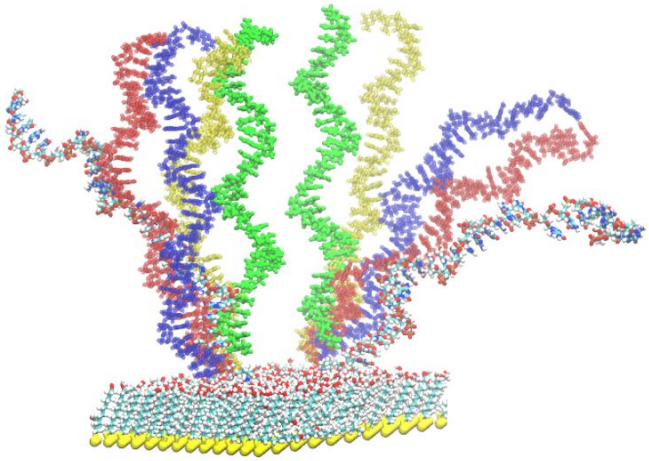

Figure 14. Snapshots from the 100 ns simulation of two probes separated by 25Å on the OH-SAM showing clear changes in orientation compared to the isolated probe on the same surface. Conformations are shown at 0 ns and every 25 ns thereafter in different colors at each time for clarity in the order: green, yellow, blue, red, and finally multi-color.

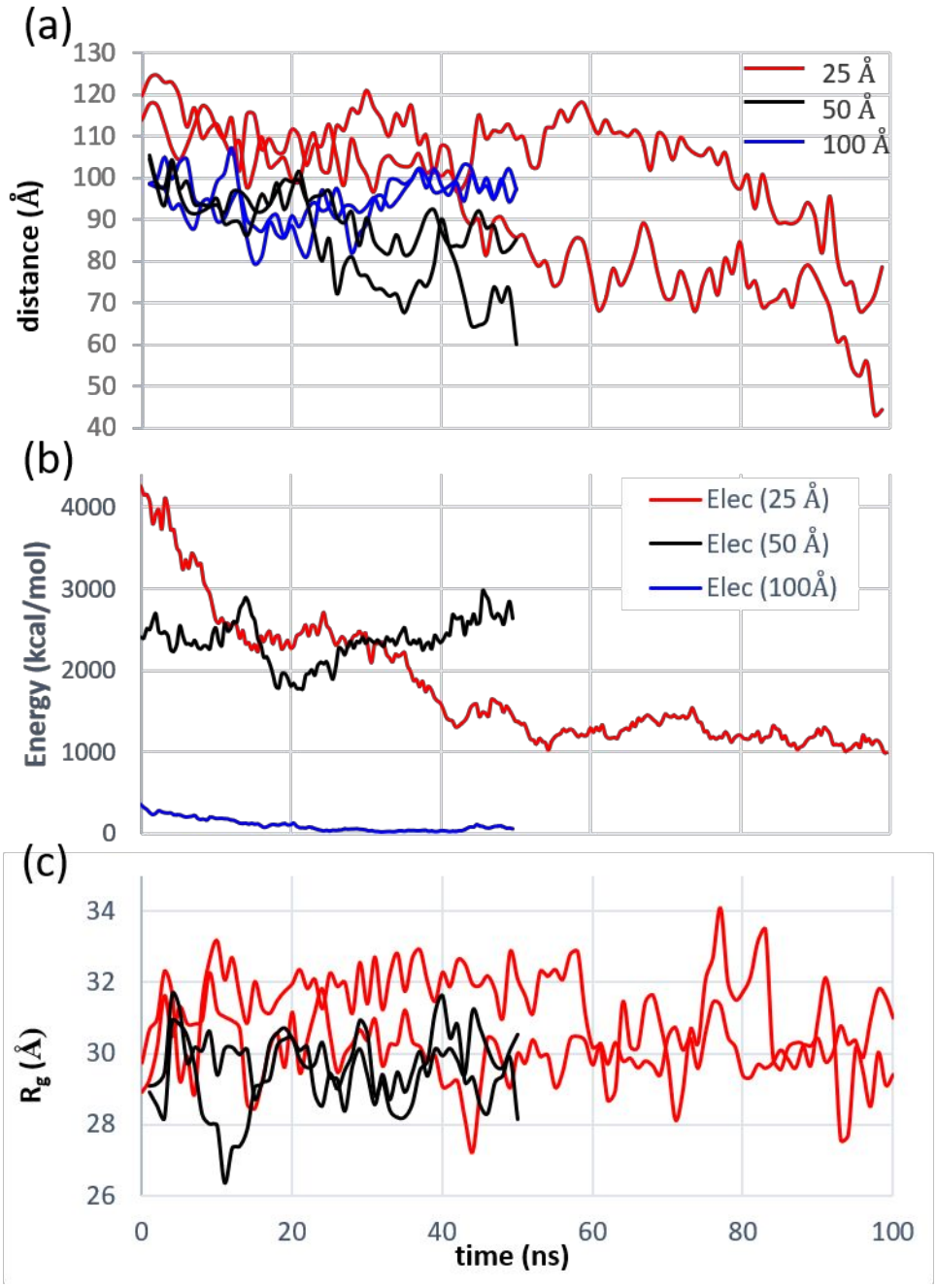

Figure 15. a) distance from probe tip to SAM for two probes at different separation distances; distances are plotted in the same color for both probes in a given simulation. b) Electrostatic interaction energy between the two probes for each separation distance. c) R_g for the two probes at the different separation distances. R_g at the 100Å separation was not calculated since no difference from isolated probes was apparent at that distance.

	Simulation Type	SAM	ssDNA Length (bases)	Time (ns)
1	Probe	C11 CH_3	29	100
2	Probe	C11 OH	29	100
3	Probe	C11 NH	29	100
4	Probe	C11 COO	29	100
5	Target 5Å distance	C11 & C16 CH_3	8	50
6	Target 5Å distance	C11 & C16 OH	8	50
7	Target 5Å distance	C11 & C16 NH	8	50
8	Target 5Å distance	C11 & C16 COO	8	50
9	Target 40Å distance	C11 CH_3	12	100
10	Target 40Å distance	C11 OH	12	100
11	Target 40Å distance	C11 NH	12	100
12	Target 40Å distance	C11 COO	12	100
13	Two probes, 25Å separation	C11 OH	29	100
14	Two probes, 50Å separation	C11 OH	29	50
15	Two probes, 100Å separation	C11 OH	29	50

Table 1. Summary of all simulations run. “Target 5Å distance” refers to the ssDNA target being started 5Å above the SAM, likewise for 40Å.

	Diffusion Coefficient ($\times 10^{-7}$ cm^2 s^{-1})				
	COO	NH	CH_3	OH	Water
C11	0.914 (0.441)	0.203 (0.0645)	8.10 (1.18)	n/a	5.62 (2.37)
C16	1.77 (0.514)	0.540 (0.100)	5.93 (2.77)	2.91 (0.750)	

Table 2. Surface diffusion coefficients of the center of mass of an 8-base ssDNA target on various SAMs and in bulk water. Values are the mean of two repeated simulations, with standard error in parentheses.

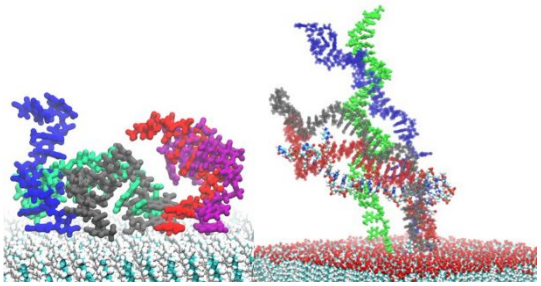

Simulations reveal dynamic properties of freely-diffusing and surface-tethered ssDNA on self-assembled monolayers with widely varying surface properties.